



## Article

# Exploring the Capability of Cu-MoS<sub>2</sub> Catalysts for Use in Electrocatalytic Overall Water Splitting

Aviraj M. Teli <sup>1</sup>, Rajneesh Kumar Mishra <sup>2,\*</sup>, Jae Cheol Shin <sup>1</sup> and Wookhee Jeon <sup>3,\*</sup>

<sup>1</sup> Division of Electronics and Electrical Engineering, Dongguk University-Seoul, Seoul 04620, Republic of Korea; avteli.teli@gmail.com (A.M.T.); jcshin@dgu.ac.kr (J.C.S.)

<sup>2</sup> Department of Physics, Yeungnam University, Gyeongsan 38541, Gyeongbuk, Republic of Korea

<sup>3</sup> Department of Semiconductor, Convergence Engineering, Sungkyunkwan University, Suwon 16419, Gyeonggi, Republic of Korea

\* Correspondence: rajneeshmishra08@gmail.com (R.K.M.); wookie92@skku.edu (W.J.)

**Abstract:** Herein, we prepare MoS<sub>2</sub> and Cu-MoS<sub>2</sub> catalysts using the solvothermal method, a widely accepted technique for electrocatalytic overall water-splitting applications. TEM and SEM images, standard tools in materials science, provide a clear view of the morphology of Cu-MoS<sub>2</sub>. HRTEM analysis, a high-resolution imaging technique, confirms the lattice spacing, lattice plane, and crystal structure of Cu-MoS<sub>2</sub>. HAADF and corresponding color mapping and advanced imaging techniques reveal the existence of the Cu-doping, Mo, and S elements in Cu-MoS<sub>2</sub>. Notably, Cu plays a crucial role in improving the hydrogen evolution reaction (HER) and oxygen evolution reaction (OER) of the Cu-MoS<sub>2</sub> catalyst as compared with the MoS<sub>2</sub> catalyst. In addition, the Cu-MoS<sub>2</sub> catalyst demonstrates significantly lower overpotential (167.7 mV and 290 mV) and Tafel slopes (121.5 mV dec<sup>-1</sup> and 101.5 mV dec<sup>-1</sup>), standing at -10 mA cm<sup>-2</sup> and 10 mA cm<sup>-2</sup> for HER and OER, respectively, compared to the MoS<sub>2</sub> catalyst. Additionally, the Cu-MoS<sub>2</sub> catalyst displays outstanding stability for 12 h at -10 mA cm<sup>-2</sup> of HER and 12 h at 10 mA cm<sup>-2</sup> of OER using chronopotentiometry. Interestingly, the Cu-MoS<sub>2</sub>||Cu-MoS<sub>2</sub> cell displays a lower cell potential of 1.69 V compared with the MoS<sub>2</sub>||MoS<sub>2</sub> cell of 1.81 V during overall water splitting. Moreover, the Cu-MoS<sub>2</sub>||Cu-MoS<sub>2</sub> cell shows excellent stability when using chronopotentiometry for 18 h at 10 mA cm<sup>-2</sup>.

**Keywords:** Cu-MoS<sub>2</sub>; HER; OER; overall water splitting; excellent stability



**Citation:** Teli, A.M.; Mishra, R.K.; Shin, J.C.; Jeon, W. Exploring the Capability of Cu-MoS<sub>2</sub> Catalysts for Use in Electrocatalytic Overall Water Splitting. *Micromachines* **2024**, *15*, 876. <https://doi.org/10.3390/mi15070876>

Academic Editor: Hong Li

Received: 3 June 2024

Revised: 30 June 2024

Accepted: 1 July 2024

Published: 3 July 2024



**Copyright:** © 2024 by the authors. Licensee MDPI, Basel, Switzerland. This article is an open access article distributed under the terms and conditions of the Creative Commons Attribution (CC BY) license (<https://creativecommons.org/licenses/by/4.0/>).

## 1. Introduction

The rapidly growing urban landscape, defense industry, space divisions, and fossil fuel-based transportation sectors are causing global warming and disparities in the ecological system [1]. Therefore, the inescapable energy shortage and ecological concerns due to carbon emissions have unlocked an opportunity for widespread research on alternative energy sources [2,3]. Hydrogen, a widely distributed substance in the universe that is generated from various catalytic nanomaterials, is comprehensively accepted as a favorable energy source with which to substitute fossil fuels [4]. Furthermore, clean and green hydrogen can be achieved using the electrochemical splitting of water, without any further carbon secretion during the hydrogen and oxygen generation process [5]. Therefore, catalytic water splitting is considered an important and vital procedure for harvesting clean hydrogen energy from chemical energy [6], consisting of two half-cell reactions at the cathode (hydrogen evolution reaction, HER) and at the anode (oxygen evolution reaction, OER) [7]. Interestingly, OER provides electrons and protons for a reduction in half-reaction, creating major energy losses due to sluggish reaction kinetics [8]. Remarkably, the OER electrocatalysts with the greatest catalytic activities are precious metals and their oxides, namely Ru, RuO<sub>2</sub>, IrO<sub>2</sub>, and Ir [9]. However, the precious metal Pt is considered the standard electrocatalyst for HER, which is expensive and makes hydrogen generation overpriced [10]. Therefore, making progress in developing active, inexpensive, durable,

and excellent conductive bifunctional catalysts for the HER and OER is one of the crucial tasks for several electrocatalytic water-splitting technologies. Curiously, numerous nanostructural materials have been studied to examine the capabilities of electrochemical water-splitting activities.

Molybdenum disulfide ( $\text{MoS}_2$ ) is a prominent member of the transition metal dichalcogenide (TMD) family that has received noteworthy attention in recent years due to its intriguing physical, optoelectronic, mechanical, and magnetic features, and various potential applications [11]. As a nanolayered material,  $\text{MoS}_2$  displays an exclusive S-Mo-S sandwich structure, where molybdenum atoms are sandwiched between layers of sulfur atoms, exhibiting an n-type behavior [12,13]. This sandwich structure of the  $\text{MoS}_2$  divulges resilient edge active sites, which facilitate quick catalytic reaction kinetics, making it a more suitable candidate for electrocatalytic water-splitting technological developments [14].  $\text{MoS}_2$  materials are multidimensional and outstanding and well recognized for their excellent optoelectronic, magnetic, mechanical, and ionic properties [15].  $\text{MoS}_2$  is an extremely stable nanomaterial with weak van der Waals interactions between the layers and resilient in-plane covalent bonds that enable smooth mechanical exfoliation into thin sheets [16]. Interestingly, the exclusive features of  $\text{MoS}_2$ , exhibited mainly when reduced to a few layers or a monolayer, facilitate its use in next-generation cutting-edge technologies.  $\text{MoS}_2$  exhibits distinct optical bandgap properties depending on its thickness. The electronic properties of the  $\text{MoS}_2$  are remarkable due to its switchable nature from an indirect bandgap (bulk form) to a direct bandgap (monolayer), which can be favorable for numerous applications. Moreover,  $\text{MoS}_2$  has an indirect bandgap of nearly 1.27 eV in the bulk form [17]. Besides,  $\text{MoS}_2$  displays a direct bandgap of about 1.90 eV in the few-layer or monolayer form [18]. The morphologies of  $\text{MoS}_2$  can differ significantly based on the synthesis techniques, which tune its properties and appropriateness in different applications.  $\text{MoS}_2$  can be synthesized in various forms, including nanotubes [19], nanosheets [20], nanoflowers [21], nanowires [14], and nanoribbons [22], each demonstrating unique edge structures, surface areas, and electrolysis water-splitting activities [23]. The morphologies of  $\text{MoS}_2$  play a decisive role in shaping its capabilities in various applications, such as the electrolysis of water [24], supercapacitors [25], field-effect transistors [26], batteries [27], perovskite light-emitting diode [28], and gas sensors [29]. Numerous production methods have been established to prepare  $\text{MoS}_2$  with precise morphologies and properties, which include hydrothermal qualities [30], solvothermal qualities [31], sol-gel applications [32], co-precipitation [33], pulse laser deposition [34], DC sputtering [35], and flame spray pyrolysis [36]. Interestingly, the above-discussed techniques offer distinctive benefits in terms of ease, scalability, and the capacity to modify the features of  $\text{MoS}_2$ . Remarkably, chemical synthesis routes, such as hydrothermal and solvothermal approaches, have been extensively used for their capability to synthesize high-purity  $\text{MoS}_2$  with well-defined morphologies [37,38]. On the other hand, physical synthesis methods, such as RF sputtering and chemical vapor deposition, have been broadly utilized to prepare high-purity  $\text{MoS}_2$  thin films in vertically aligned morphologies with various applications [39,40]. Despite its prospective applications,  $\text{MoS}_2$  faces serious limitations, such as slow OER electrocatalytic reaction kinetics, high overpotential, and inadequate stability, which hamper its commercial applicability. Therefore, improving the catalytic performance of  $\text{MoS}_2$  is imperative for its practical application. Among the various doping materials investigated, copper (Cu) is a hopeful catalytic candidate for advancing the electrochemical activities of the  $\text{MoS}_2$ . Therefore, the Cu-doped  $\text{MoS}_2$  ( $\text{Cu-MoS}_2$ ) boosts ionic interactions, magnifies the surface area, and enables electrical conduction, making it predominantly active in increasing electrocatalytic activities. Therefore, the doping of Cu into  $\text{MoS}_2$  can build chemically active defect states, which can increase overall conductivity, thereby regulating the overall water-splitting process.

In this work, we investigate the electrocatalytic overall water splitting of the  $\text{MoS}_2$  and  $\text{Cu-MoS}_2$  catalysts. Fascinatingly, the  $\text{MoS}_2$  and  $\text{Cu-MoS}_2$  catalysts are prepared using a simple, scalable, and inexpensive solvothermal method. Attractively, Cu plays a dynamic role in ornamenting the electrocatalytic overall water-splitting properties of the  $\text{Cu-MoS}_2$

catalyst. Stimulatingly, the Cu-MoS<sub>2</sub> catalyst shows a low overpotential and a low Tafel slope of HER and OER compared to the MoS<sub>2</sub> catalyst. Fascinatingly, Cu-MoS<sub>2</sub>||Cu-MoS<sub>2</sub> cell shows low potential and excellent stability for 18 h at 10 mA cm<sup>-2</sup>. Moreover, the OER and HER mechanisms are also discussed to study the reaction process of hydrogen and oxygen generation.

## 2. Synthesis Methods

MoS<sub>2</sub> and Cu-MoS<sub>2</sub> were prepared using a straightforward one-step solvothermal process. Typically, 60 mL (1:1 ratio) of ethanol and DI water were mixed with 16 mg of C<sub>2</sub>H<sub>5</sub>NS and 4 mmol of Na<sub>2</sub>MoO<sub>4</sub>·2H<sub>2</sub>O, while being magnetically stirred to create a consistent solution. Furthermore, 2 mg of Cu was melted in 10 mL of DI water using a combination of magnetic stirring and sonication. Further, using magnetic stirring, 3 mL of the Cu precursor was gradually mixed dropwise into the 60 mL Mo and S precursor solution. The Mo and S precursor solution, mixed with Cu, was then shifted to an autoclave with a capacity of 100 milliliters. Additionally, a 2.2 cm × 3.0 cm portion of washed Ni-foam was put in the autoclave at 180 °C for 18 h to allow Cu-MoS<sub>2</sub> to grow in situ on 3D Ni-foam. Finally, the Cu-MoS<sub>2</sub> deposited on Ni-foam was washed with ethanol and DI water to remove the impurities and dehydrated at 95 °C under vacuum conditions for 15 h. Similarly, pure MoS<sub>2</sub> was also synthesized using the above-discussed method with a Cu source.

The Cu-MoS<sub>2</sub> morphology of the Ni-foam is meticulously scanned via a scanning electron microscope (SEM) obtained from S-4800 HITACHI, Ltd., Tokyo, Japan. Additionally, the structural, morphological, and elemental properties of the Cu-MoS<sub>2</sub> are thoroughly studied via TEM, HRTEM, and HAADF with elemental mapping using the JEOL, JEM-2100F, JEOL Ltd., Tokyo, Japan. Moreover, the electrocatalytic activities of the MoS<sub>2</sub> and Cu-MoS<sub>2</sub> catalysts for electrocatalytic water splitting are rigorously tested using the electrochemical workstation VersaSTAT3 (Princeton Applied Research). The electrocatalytic performances of the MoS<sub>2</sub> and Cu-MoS<sub>2</sub> electrocatalysts are tested via a three-electrode arrangement in a 1.0 M KOH alkaline electrolyte. The MoS<sub>2</sub> and Cu-MoS<sub>2</sub> catalysts, Pt, and Ag/AgCl are used as working, counter, and reference electrodes, respectively. The overall water splitting is investigated in two-electrode arrangements in 1.0 M KOH, where MoS<sub>2</sub> or Cu-MoS<sub>2</sub> are used in both anode and cathode electrodes. The linear sweep voltammetry (LSV) of the MoS<sub>2</sub> and Cu-MoS<sub>2</sub> catalysts are studied at 5 mV s<sup>-1</sup>. Furthermore, the Tafel slopes of the MoS<sub>2</sub> and Cu-MoS<sub>2</sub> catalysts are accomplished from the LSV plot, using  $\eta = b \log j + a$ , where  $b$  is the Tafel slope,  $j$  is the current density,  $a$  is the transfer coefficient, and  $\eta$  is the overpotential. The recorded potential vs. Ag/AgCl is converted into the potential of the reversible hydrogen electrode (RHE) via the relation  $E_{RHE} = E_{Ag/AgCl}^0 + E_{Ag/AgCl} + 0.059 \times pH$ .

## 3. Results and Discussions

Figure 1 elucidates the scanning electron microscopy (SEM) visuals of the Cu-MoS<sub>2</sub>. The shape of the Cu-MoS<sub>2</sub> grown on the Ni-foam substrate is shown in Figure 1a,b at different magnifications, exploring the different orientations of the nanolayers. Further, the nanolayered morphology of Cu-MoS<sub>2</sub> is described in Figure 1a,b, where the outermost portions of the nanolayers can be seen in various directions, enabling a greater chance for engagement with the alkaline electrolyte, which can be beneficial for improving the electrocatalytic water-splitting activities. Also, the surface area of Cu-MoS<sub>2</sub> can be significantly expanded by these multilayered architectures, and thus, these unique nanolayer structures create ideal sites of interaction on the Cu-MoS<sub>2</sub> surface for hydrogen and oxygen evolution reaction procedures. Moreover, Cu-doping in Cu-MoS<sub>2</sub> boosts the number of engaged reaction sites and their area of interface with the KOH electrolyte, which can enhance the catalytic capabilities of the hydrogen and oxygen evolution reaction. In addition, this unique Cu-MoS<sub>2</sub> morphology can also promote the transfer of electrons due to the highly conductive nature of Cu in the Cu-MoS<sub>2</sub>. However, the surface structure of

the Cu-MoS<sub>2</sub> also indicates that it is able to transfer hydrogen and oxygen molecules and improve adsorption and desorption to accelerate kinetics for the development of hydrogen and oxygen in overall water splitting.

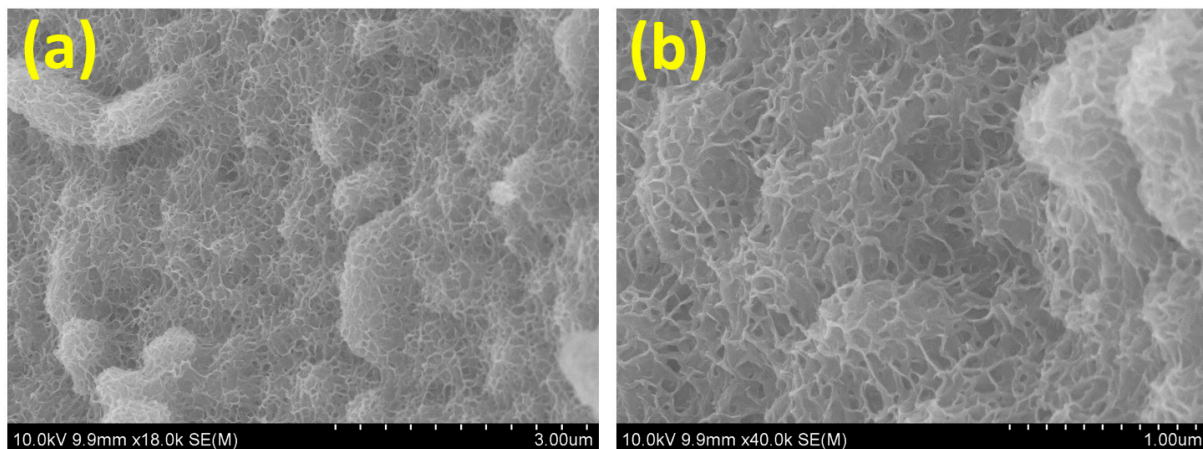


**Figure 1.** (a,b) The SEM pictures of the Cu-MoS<sub>2</sub> on 3D Ni-foam at different magnifications.

Additionally, Figure 2a,b depict the transmission electron microscopy (TEM) images of the Cu-MoS<sub>2</sub> to further study morphology on the nanoscale at different magnifications. It is observed that the synthesized Cu-MoS<sub>2</sub> illustrates the agglomerated nanolayers. It is also important that the nanoscale shape of the Cu-MoS<sub>2</sub> plays a significant role in the creation of the catalytically active sites on the catalyst surface, which can be beneficial for overall water-splitting applications. Interestingly, crumbled nanolayers of Cu-MoS<sub>2</sub> also offer more exposure area for the KOH electrolyte during oxygen, hydrogen, and overall water-splitting tests. Consequently, it is expected that the TEM images will support the SEM results, as depicted in Figure 1. Furthermore, the structural examination of the Cu-MoS<sub>2</sub> is studied using high-resolution TEM (HRTEM) and FFT, as portrayed in Figure 3a–e. Figure 3a shows the HRTEM image of the Cu-MoS<sub>2</sub>, illustrating several small crystallites, which show the lattice fringes of the Cu-MoS<sub>2</sub>. Interestingly, these small crystallites merge together to form the nanolayers of Cu-MoS<sub>2</sub>, which have a significant impact on the creation of various lattice strains in the Cu-MoS<sub>2</sub> nanolayers. Figure 3b,d display the zoomed portion of the HRTEM image of Cu-MoS<sub>2</sub> to reveal 0.265 nm lattice spacing. Figure 3c,e present the FFT images of the Cu-MoS<sub>2</sub> from the HRTEM area, as shown in Figure 3b,d. The FFT images of the Cu-MoS<sub>2</sub> show the lattice plane (100) corresponding to 0.265 nm lattice spacing. Moreover, the lattice spacing (0.265 nm) and lattice plane (100) of the synthesized Cu-MoS<sub>2</sub> are consistent with those of the JCPDS card no. 37-1492, which confirms the hexagonal crystal structure [41]. In addition, to verify the Cu-doping, color mapping of the Cu-MoS<sub>2</sub> is performed and the results are shown in Figure 4a–d. Figure 4a reveals the high-angle annular dark field-scanning (HAADF) image of the Cu-MoS<sub>2</sub>, which is used for the color mapping of Mo, S, and Cu elements. Figure 4b–d exhibit the color mapping of Cu, Mo, and S elements, which confirms the doping of Cu atoms in the Cu-MoS<sub>2</sub>.

The oxygen evolution reaction (OER) has a high energy barrier for its four-electron transfer mechanism, hindering the rate of electrocatalytic reaction kinetics. The electrochemical performance of the MoS<sub>2</sub> and Cu-MoS<sub>2</sub> electrocatalysts for OER is studied by a three-electrode arrangement in a 1.0 M KOH alkaline medium. Figure 5a depicts the linear sweep voltammetry (LSV) plots, comparing the characteristics of the MoS<sub>2</sub> and Cu-MoS<sub>2</sub> catalysts at 5 mV s<sup>−1</sup>. The LSV plots noticeably elucidate that the Cu-MoS<sub>2</sub> catalyst reveals remarkably higher OER performances than the MoS<sub>2</sub> catalyst. Moreover, Figure 5b divulges the overpotentials of the Cu-MoS<sub>2</sub> and MoS<sub>2</sub> electrocatalysts. Stimulatingly, the Cu-MoS<sub>2</sub> catalyst specifies a smaller overpotential of 290 mV than the MoS<sub>2</sub> catalyst of 380 mV. This reduction in the overpotential of the Cu-MoS<sub>2</sub> electrocatalyst is due to the doping of Cu, which improves electron transport and favorable adsorption energies and reduces the

energy barrier during the OER process [42,43]. Figure 5c elucidates the Tafel plots of the Cu-MoS<sub>2</sub> and MoS<sub>2</sub> electrocatalysts to examine the reaction rate kinetics. It is observed that the Tafel slope of the Cu-MoS<sub>2</sub> electrocatalyst is 101.5 mV dec<sup>-1</sup>, which is smaller than that of the MoS<sub>2</sub> electrocatalyst at 106.3 mV dec<sup>-1</sup>. In addition, Figure 5d discloses results of a stability test performed to estimate the robustness of the Cu-MoS<sub>2</sub> catalyst. It is observed that the initial potential of stability of the Cu-MoS<sub>2</sub> catalyst is 1.52 V, which upsurges to 1.54 V after 12 h of the chronopotentiometry test at a current density of 10 mA cm<sup>-2</sup>. The outstanding stability of the Cu-MoS<sub>2</sub> electrocatalyst is due to its various features, such as the strong interaction between the Cu-doping atom and host MoS<sub>2</sub>, the high surface area, its low susceptibility to structural breakdown, and the decreased deactivation of the active sites on the Cu-MoS<sub>2</sub> electrocatalyst surface [44,45]. The structural stability, such as mechanical stress; well-created active sites; lack of significant degradation during the long-term stability test for 12 h; and excellent thermal stability of the nanolayered Cu-MoS<sub>2</sub> catalyst were significant [46,47].

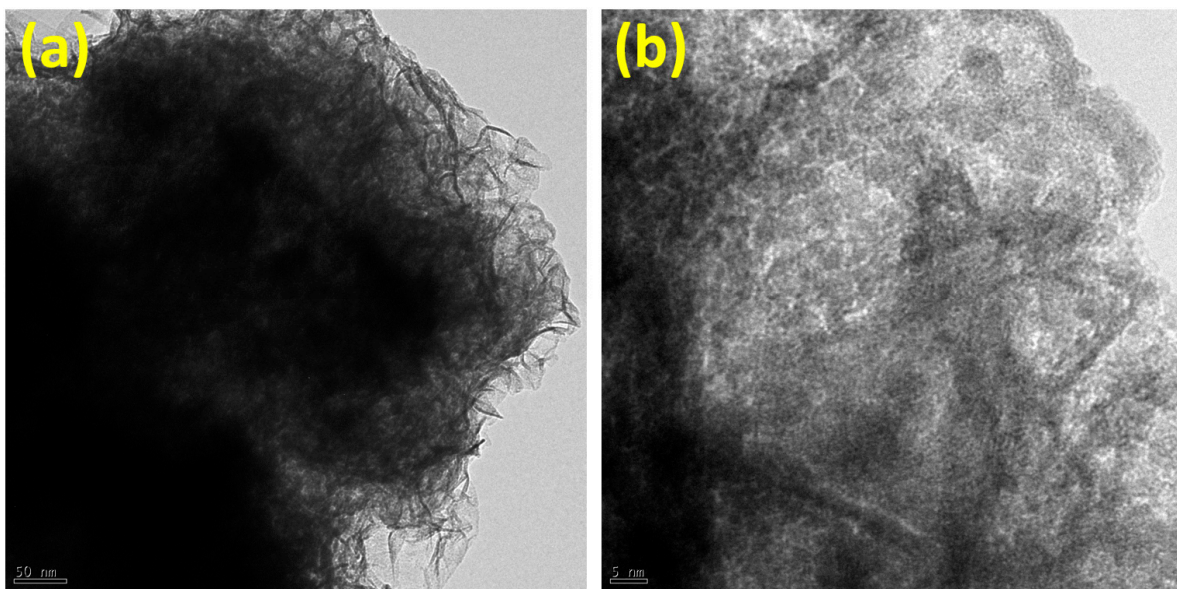


Figure 2. (a,b) TEM images of the Cu-MoS<sub>2</sub> at different magnifications.

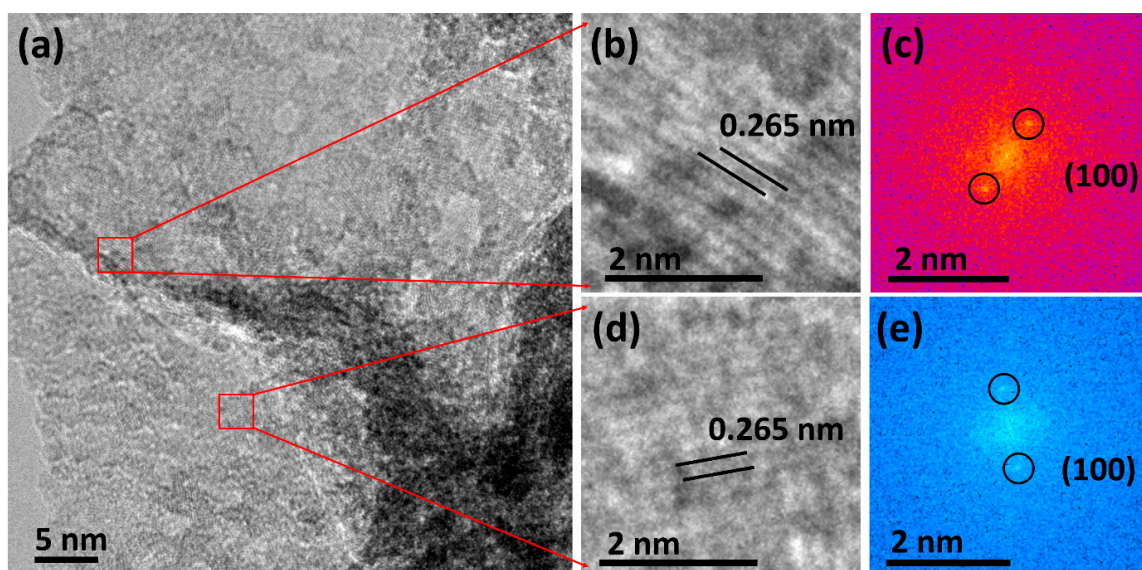
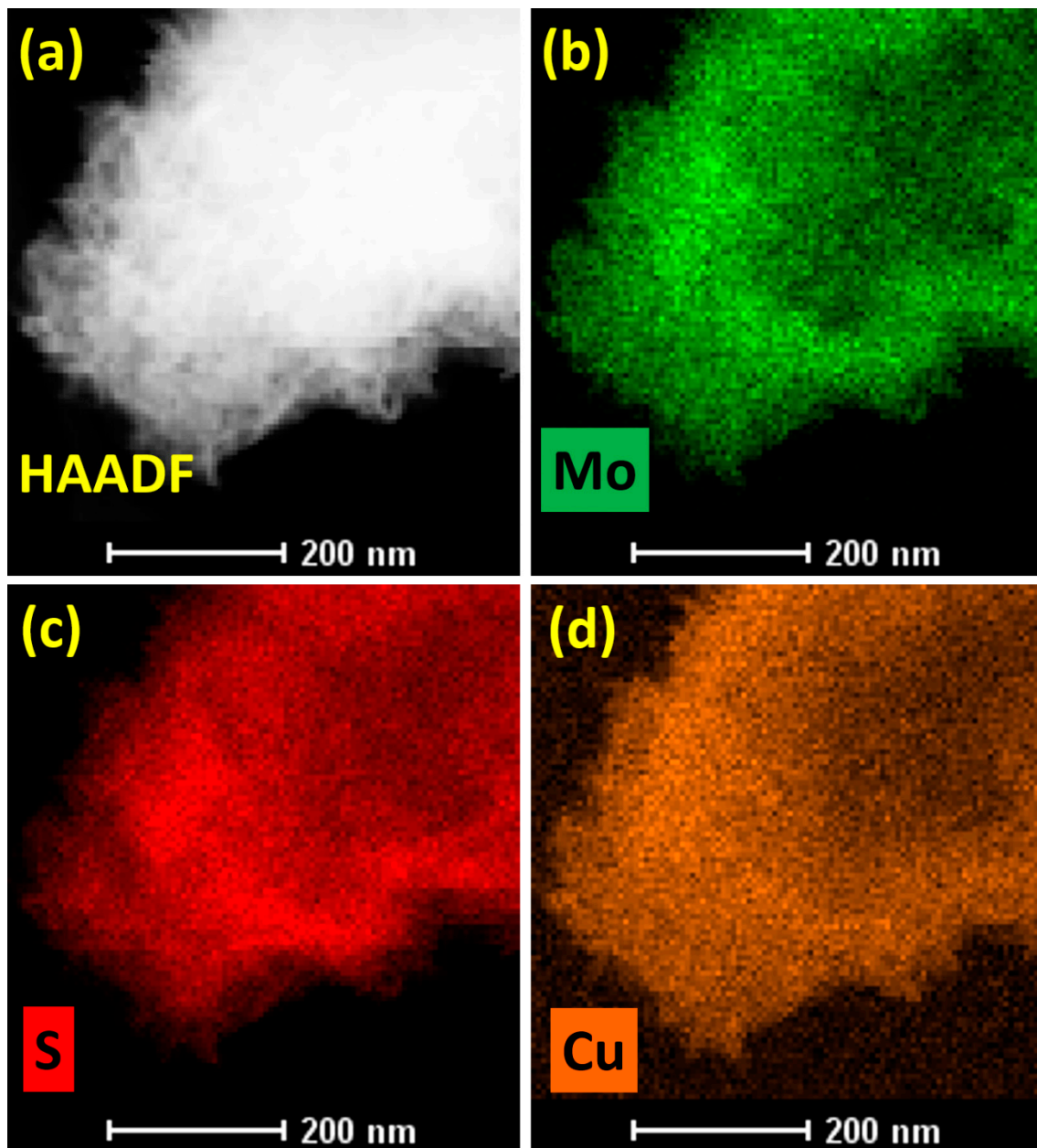


Figure 3. (a) HRTEM image, (b,d) HRTEM images from the enlarged area, and corresponding (c,e) FFT patterns of the Cu-MoS<sub>2</sub>.



**Figure 4.** (a) HAADF image and elemental mapping of (b) Mo, (c) S, and (d) Cu elements of the Cu-MoS<sub>2</sub>.

The HER catalytic activities of the Cu-MoS<sub>2</sub> and MoS<sub>2</sub> electrocatalysts are investigated using the simple three-electrode process in an alkaline 1.0 M KOH. Figure 6a displays the linear sweep voltammetry (LSV) plots of the MoS<sub>2</sub> and Cu-MoS<sub>2</sub> catalysts at a scan rate of 5 mV s<sup>-1</sup>. As depicted in the LSV plots in Figure 6a, the Cu-MoS<sub>2</sub> catalyst unveils superior hydrogen evolution activities to the MoS<sub>2</sub> catalyst. Interestingly, the onset potential of the Cu-MoS<sub>2</sub> catalyst is lower than that of the MoS<sub>2</sub> catalyst, which necessitates low energy use to initiate the electrocatalytic hydrogen evolution reaction [48,49]. Therefore, it is expected that the Cu-MoS<sub>2</sub> catalyst can offer a greater rate of hydrogen generation than the MoS<sub>2</sub> catalyst at the same applied potential. Further, Figure 6b presents overpotential plots of the MoS<sub>2</sub> and Cu-MoS<sub>2</sub> catalysts, providing vital insight into their electrocatalytic efficiency. The Cu-MoS<sub>2</sub> catalyst illustrates a lower overpotential of 167.7 mV than the MoS<sub>2</sub> catalyst, which has one of 193.4 mV. It is supposed that the Cu-doping might be responsible for the increased presence of active sites on the Cu-MoS<sub>2</sub> electrocatalyst surface [50]. Also, Cu-

doping in MoS<sub>2</sub> can create structural changes in the electronic properties of the Cu-MoS<sub>2</sub> catalyst, leading to reduced overpotential [42]. Fascinatingly, Tafel slopes are vital factors in electrocatalytic hydrogen evolution reactions, offering insightful indications regarding the reaction kinetics and mechanism [51]. Figure 6c elucidates the Tafel plots of the Cu-MoS<sub>2</sub> and MoS<sub>2</sub> electrocatalysts to examine their reaction rate kinetics and mechanisms. It is observed that the Tafel slope value of the Cu-MoS<sub>2</sub> electrocatalyst is lower, at 121.5 mV dec<sup>-1</sup>, than that of the MoS<sub>2</sub> catalyst at 124.4 mV dec<sup>-1</sup>. This reduces the Tafel slope value of the Cu-MoS<sub>2</sub> catalyst, suggesting that low overpotential is necessary to reach  $-10 \text{ mA cm}^{-2}$ . Interestingly, the doping of the Cu atom can increase the electron transfer capability of the Cu-MoS<sub>2</sub> electrocatalyst and further lower the energy barrier during the HER process. Moreover, Figure 6d reveals the results of a stability test of the Cu-MoS<sub>2</sub> catalyst, performed to inspect its durability at  $-10 \text{ mA cm}^{-2}$ . Using the chronopotentiometry test, it is observed that the initial potential of the Cu-MoS<sub>2</sub> electrocatalyst is 166.8 mV, and it reaches up to 173.2 mV after 12 h of stability. Excitingly, it can be the intrinsic properties of the 2D-layered Cu-MoS<sub>2</sub> catalyst, such as outstanding chemical stability, surface area, and resistance to corrosion, which influence the adsorption and desorption process during the 12 h stability test [52–54].

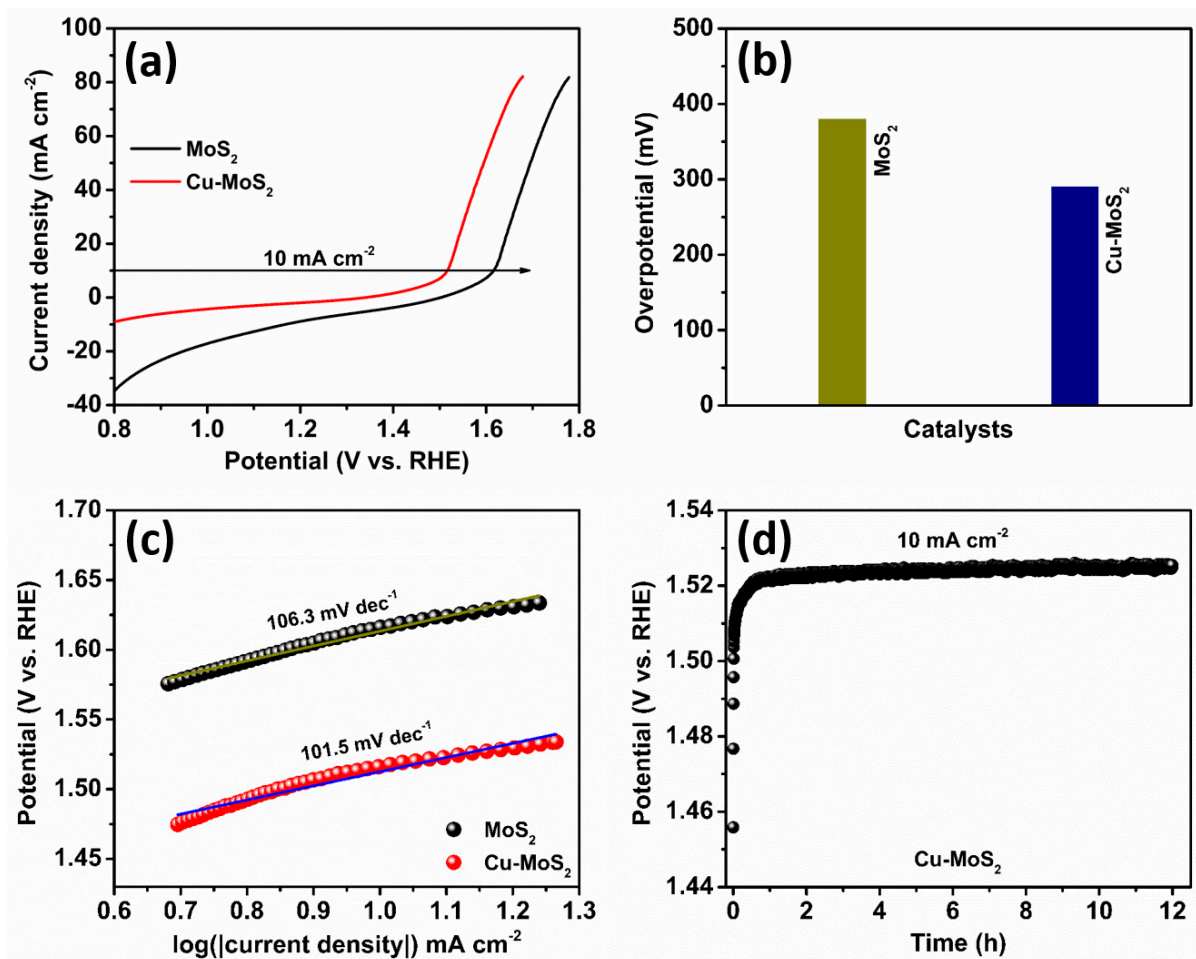


**Figure 5.** Electrocatalytic oxygen evolution reaction (OER). (a) LSV plots, (b) overpotential, and (c) Tafel plots of the MoS<sub>2</sub> and Cu-MoS<sub>2</sub> catalysts. (d) Stability test of the Cu-MoS<sub>2</sub> catalyst at  $10 \text{ mA cm}^{-2}$  for 12 h.

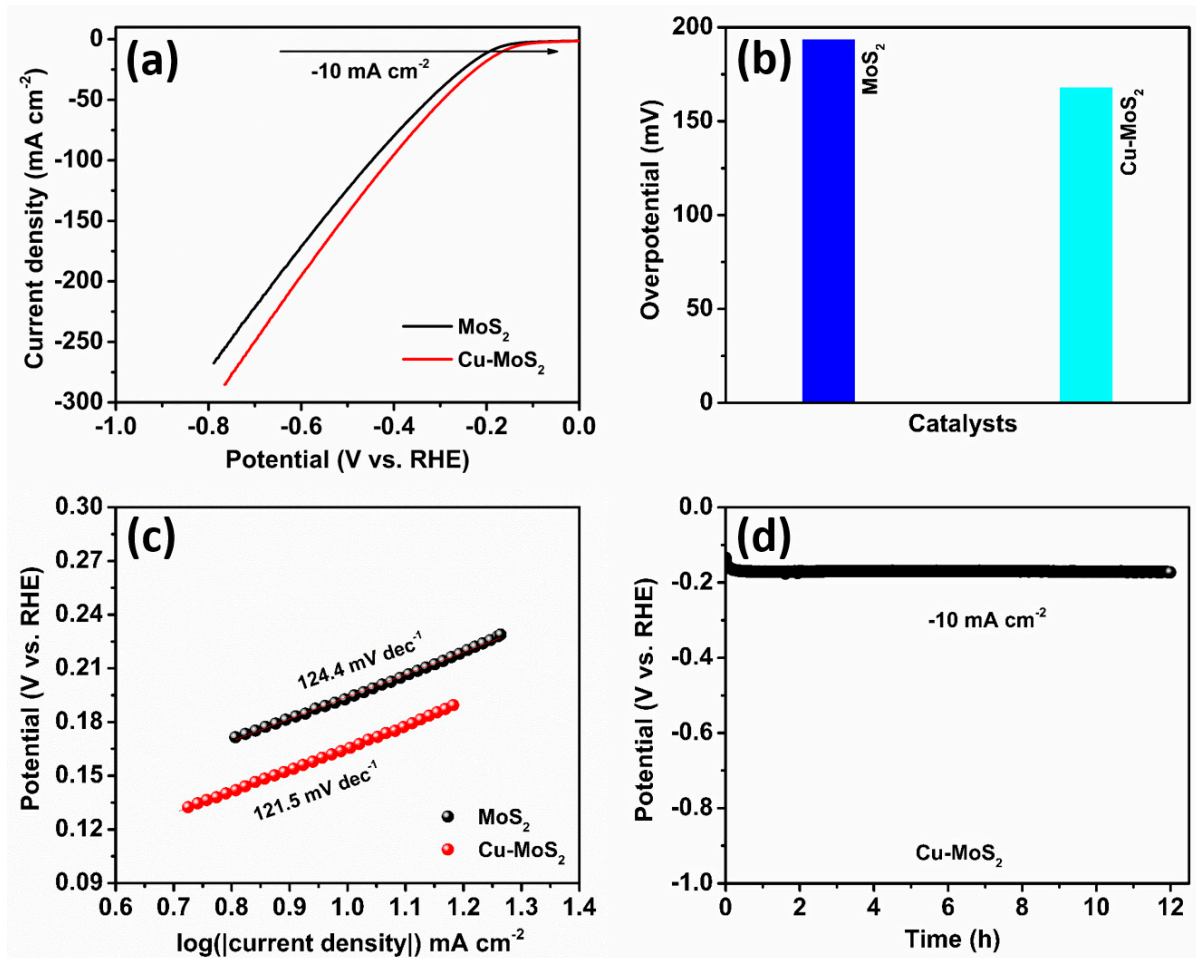


**Figure 6.** Electrochemical hydrogen evolution reaction (HER). (a) LSV plots, (b) overpotential, and (c) Tafel plots of the MoS<sub>2</sub> and Cu-MoS<sub>2</sub> catalysts. (d) Stability test of the Cu-MoS<sub>2</sub> catalyst at  $-10 \text{ mA cm}^{-2}$  for 12 h.

Further, we investigated the electrocatalytic activities of the MoS<sub>2</sub>||MoS<sub>2</sub> cell and Cu-MoS<sub>2</sub>||Cu-MoS<sub>2</sub> cell in a two-electrode arrangement (overall water splitting) in 1.0 M KOH alkaline. Figure 7a displays the linear sweep voltammetry (LSV) plots of the MoS<sub>2</sub>||MoS<sub>2</sub> cell and Cu-MoS<sub>2</sub>||Cu-MoS<sub>2</sub> cell at  $5 \text{ mV s}^{-1}$  in overall water splitting. It is observed that Cu-doping in the MoS<sub>2</sub> plays a significant role in the shift of the LSV curve toward the low-potential side. Figure 7b displays the cell potential in the overall water splitting of the MoS<sub>2</sub>||MoS<sub>2</sub> cell and Cu-MoS<sub>2</sub>||Cu-MoS<sub>2</sub> at  $10 \text{ mA cm}^{-2}$ . Fascinatingly, the Cu-MoS<sub>2</sub>||Cu-MoS<sub>2</sub> cell shows a small cell potential of 1.69 V compared to the MoS<sub>2</sub>||MoS<sub>2</sub> cell's potential of 1.81 V in overall water splitting. The low cell potential of the Cu-MoS<sub>2</sub>||Cu-MoS<sub>2</sub> cell compared with MoS<sub>2</sub>||MoS<sub>2</sub> cell is ascribed to the synergistic influence of Cu-doping in the host MoS<sub>2</sub>. Curiously, the stability of the MoS<sub>2</sub>||MoS<sub>2</sub> cell is vital for everyday applications in overall water-splitting applications, where enduring practical productivity is essential. Figure 7c parades the stability results after 18 h of processing the Cu-MoS<sub>2</sub>||Cu-MoS<sub>2</sub> cell at a  $10 \text{ mA cm}^{-2}$  current density in an overall water-splitting process. Using the chronopotentiometry test, it is observed that the cell potential upsurges from 1.726 V to 1.75 V during 18 h of testing at  $10 \text{ mA cm}^{-2}$ . The inset in Figure 7c shows an optical photograph of the overall water splitting. Remarkably, various factors, including electrolyte composition, conductivity, ion exchange, corrosiveness, impurity atoms, and pH, affect the overall water-splitting durability of the Cu-MoS<sub>2</sub>||Cu-MoS<sub>2</sub> cell during the 18 h chronopotentiometry test. Furthermore, the doping of the Cu atom in the Cu-MoS<sub>2</sub> catalyst reduces structural degradation over 18 h of stability and enhances its surface chemistry,



which can decrease the corrosion of the catalyst, creating excellent synergy between Cu-atom and MoS<sub>2</sub> in the Cu-MoS<sub>2</sub> catalyst, improving charge-transfer, and reducing the energy required to complete the overall water-splitting reaction [55,56].

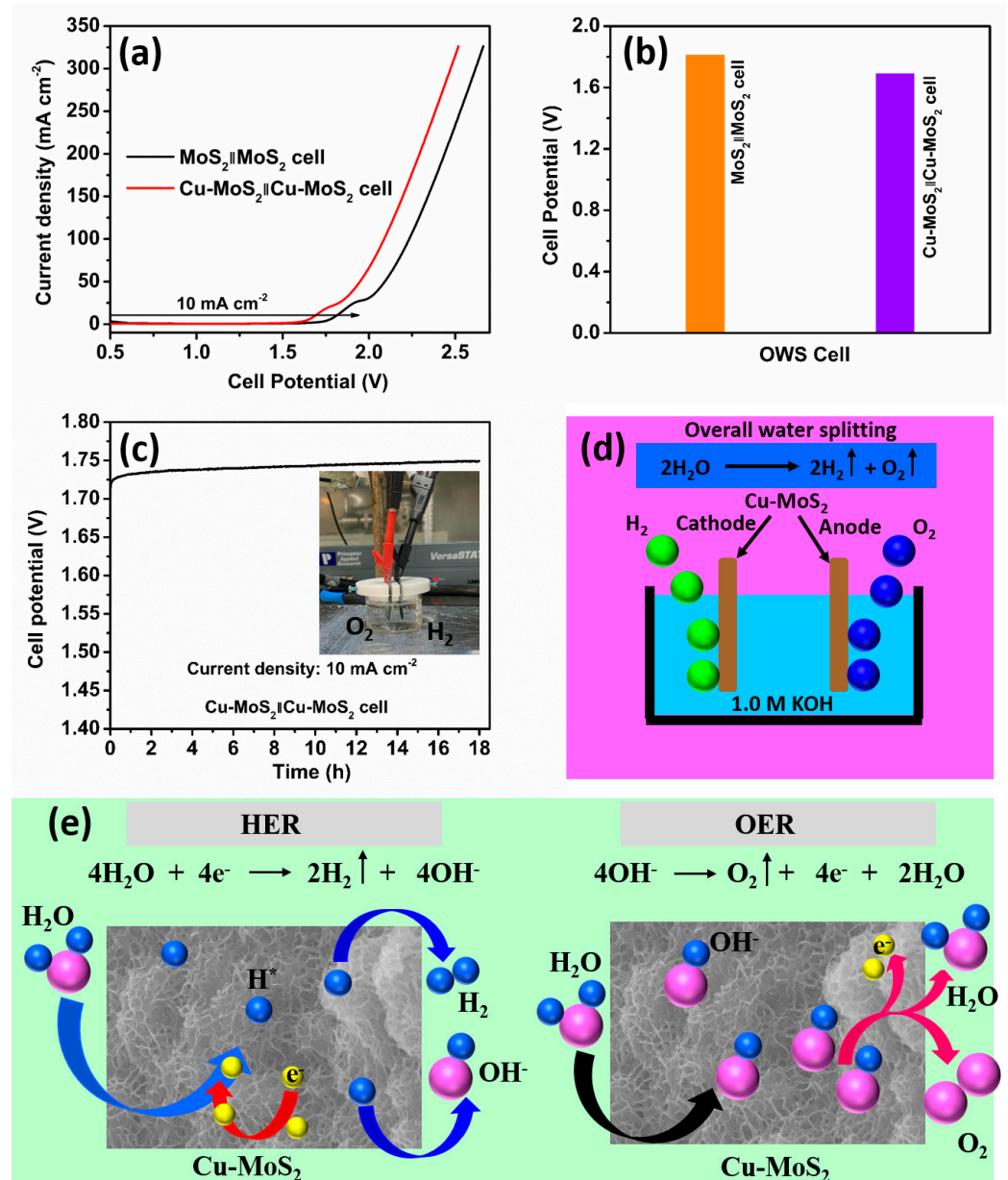


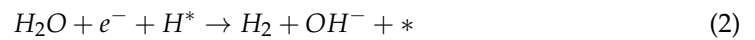
**Figure 7.** (a) LSV plots. (b) Cell potentials of the MoS<sub>2</sub>||MoS<sub>2</sub> cell and Cu-MoS<sub>2</sub>||Cu-MoS<sub>2</sub> cell. (c) Stability of the Cu-MoS<sub>2</sub>||Cu-MoS<sub>2</sub> cell at 10 mA cm<sup>-2</sup> (inset—optical photograph) and (d) schematic presentation of the overall water-splitting mechanism of the Cu-MoS<sub>2</sub>||Cu-MoS<sub>2</sub> cell. (e) Schematic depiction of the impact of the HER and OER mechanisms on the Cu-MoS<sub>2</sub> catalyst surface.

Further, in the Cu-MoS<sub>2</sub>||Cu-MoS<sub>2</sub> cell, the water-splitting mechanism implicates both the hydrogen evolution reaction (HER) and oxygen evolution reaction (OER). The HER mechanism is elaborated in the following Equations (1)–(3) [41,57] and illustrated in Figure 7e.

Volmer process:



Heyrovsky process:

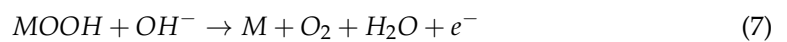


Tafel process:



Figure 7e shows the HER mechanism, which follows the Equations (1) and (2) because the Tafel slope value lies in the range of the Heyrovsky process.

Fascinatingly, the oxygen evolution reaction (OER) is sluggish, and it needs to be improved using different variations in the electrocatalysts. Generally, the OER is the adsorption four-electron transfer process. The OER takes place in various steps in alkaline electrolytes, as shown in the following, Equations (4)–(7) [58,59].



In Equation (4), the adsorption of  $OH^-$  with the active site  $M$  onto the Cu-MoS<sub>2</sub> electrocatalyst's surface generates  $OH$  and an electron. In Equation (5), the interaction between  $OH$  and  $OH^-$  of the Cu-MoS<sub>2</sub> electrocatalyst surface and then the bond-breaking process produce water molecules, oxygen, and an electron. Moreover, the second adsorption process is discussed in Equation (6), which illustrates the intermediate state  $OOH$ , making bonds with active site  $M$  on the Cu-MoS<sub>2</sub> electrocatalyst's surface. Furthermore, the intermediate state  $OOH$ , adsorbed onto the active site  $M$  on the Cu-MoS<sub>2</sub> surface, further interacts with  $OH$ , which produces water molecules, creates oxygen, and releases an electron as discussed in Equation (7). Figure 7d,e exposes the schematic illustration of the overall water splitting of the Cu-MoS<sub>2</sub>||Cu-MoS<sub>2</sub> cell. Interestingly, the graphic depiction in Figure 7d,e explores the understanding of the electrocatalytic developments occurring at both the anode (Cu-MoS<sub>2</sub>) and cathode (Cu-MoS<sub>2</sub>) electrodes in 1.0 M KOH. Unusually, protons from electrolytes are reduced at the cathode (Cu-MoS<sub>2</sub>) electrode to produce hydrogen energy. However, water molecules are oxidized at the anode (Cu-MoS<sub>2</sub>) electrode to produce oxygen, protons, and electrons. Moreover, Table 1 lists the electrocatalytic results reported works in the literature for comparison with the present study. The Cu-MoS<sub>2</sub> catalyst is observed to be better than or comparable to the reported results.

**Table 1.** Comparative study of the electrocatalytic activities of the Cu-MoS<sub>2</sub> catalyst with other results reported from the literature.

S. No.	Catalysts	Electrolyte	Overpotential	Stability	Ref.
Oxygen Evolution Reaction					
1	MoS <sub>2</sub> quantum dots	1.0 M KOH	370 mV (10 mA cm <sup>-2</sup> )	2 h (10 mA cm <sup>-2</sup> )	[60]
2	MoS <sub>2</sub> nanosheets wrapped MOF-based Co <sub>3</sub> O <sub>4</sub>	1.0 M KOH	230 mV (10 mA cm <sup>-2</sup> )	13 h (10 mA cm <sup>-2</sup> )	[61]
3	Metal-organic-framework-derived Co <sub>9</sub> S <sub>8</sub> -MoS <sub>2</sub>	1.0 M KOH	270 mV (10 mA cm <sup>-2</sup> )	24 h (10 mA cm <sup>-2</sup> )	[44]
4	MoS <sub>2</sub> -based hybrid with N-doped carbon-wrapped CoFe alloy	1.0 M KOH	337 mV (10 mA cm <sup>-2</sup> )	24 h (10 mA cm <sup>-2</sup> )	[62]
5	Cu-MoS <sub>2</sub>	1.0 M KOH	290 mV (10 mA cm <sup>-2</sup> )	12 h (10 mA cm <sup>-2</sup> )	This work

Table 1. Cont.

S. No.	Catalysts	Electrolyte	Overpotential	Stability	Ref.
Hydrogen Evolution Reaction					
6	Cu-MoS <sub>2</sub> /NiS <sub>2</sub>	1.0 M KOH	105 mV (−10 mA cm <sup>−2</sup> )	--	[42]
7	W-1T MoS <sub>2</sub> -15	0.5 M H <sub>2</sub> SO <sub>4</sub>	292 mV (−10 mA cm <sup>−2</sup> )	14 h (−10 mA cm <sup>−2</sup> )	[63]
8	Mix-phased 1 T/2 H MoS <sub>2</sub>	1.0 M KOH	145 mV (−10 mA cm <sup>−2</sup> )	24 h (−10 mA cm <sup>−2</sup> )	[64]
9	AC/MoS <sub>2</sub> -F	0.5 M H <sub>2</sub> SO <sub>4</sub>	136 mV (−10 mA cm <sup>−2</sup> )	24 h (−10 mA cm <sup>−2</sup> )	[65]
10	Cu-MoS <sub>2</sub>	1.0 M KOH	167.7 mV (−10 mA cm <sup>−2</sup> )	12 h (−10 mA cm <sup>−2</sup> )	This work
Overall water splitting					
11	CoS/MoS <sub>2</sub>    CoS/MoS <sub>2</sub>	1.0 M KOH	1.61 V (cell potential) (10 mA cm <sup>−2</sup> )	12 h (10 mA cm <sup>−2</sup> )	[66]
12	MoS <sub>2</sub> -CoFeLDH/NF    MoS <sub>2</sub> -CoFeLDH/NF	1.0 M KOH	1.55 V (cell potential) (10 mA cm <sup>−2</sup> )	48 h (10 mA cm <sup>−2</sup> )	[23]
13	MoS <sub>2</sub> /NiFe <sub>2</sub> O <sub>4</sub>    MoS <sub>2</sub> /NiFe <sub>2</sub> O <sub>4</sub>	1.0 M KOH	1.69 V (cell potential) (10 mA cm <sup>−2</sup> )	--	[67]
14	1T-MoS <sub>2</sub> /Ni <sub>3</sub> S <sub>2</sub> /LDH    1T-MoS <sub>2</sub> /Ni <sub>3</sub> S <sub>2</sub> /LDH	1.0 M KOH	1.55 V (cell potential) (10 mA cm <sup>−2</sup> )	20 h (10 mA cm <sup>−2</sup> )	[68]
15	Cu-MoS <sub>2</sub>    Cu-MoS <sub>2</sub>	1.0 M KOH	1.69 V (cell potential) (10 mA cm <sup>−2</sup> )	18 h (10 mA cm <sup>−2</sup> )	This work

#### 4. Conclusions

In conclusion, the Cu-MoS<sub>2</sub> catalyst, which is synthesized by the simple and scalable solvothermal method, shows remarkable electrocatalytic activities in the overall water-splitting application. The Cu-MoS<sub>2</sub> catalyst depicts low overpotential and small Tafel slopes during HER and OER. We also investigate whether the Cu-MoS<sub>2</sub> catalyst elucidates the outstanding stability of OER (at 10 mA cm<sup>−2</sup>) and HER (at −10 mA cm<sup>−2</sup>) in a three-electrode setup. The Cu-MoS<sub>2</sub>||Cu-MoS<sub>2</sub> cell illustrates excellent stability for 18 h and a small cell potential of 1.69 V at 10 mA cm<sup>−2</sup>. Therefore, it is concluded that the Cu-MoS<sub>2</sub>||Cu-MoS<sub>2</sub> cell shows enhanced electrocatalytic activities due to Cu doping, resulting in a lower cell potential and outstanding stability in overall water splitting, which is crucial for practical applications in renewable energy technologies. Furthermore, variations in the Cu-doping concentration, the Mo and S precursor concentrations, and the solvothermal reaction temperature and time need to be further optimized to tailor the morphology and properties of the Cu-doped MoS<sub>2</sub> for various applications, such as in sensors, memory devices, supercapacitors, batteries, and photocatalysis.

**Author Contributions:** Conceptualization, R.K.M.; Investigation, A.M.T.; Data curation, A.M.T.; Writing—review & editing, A.M.T., R.K.M., J.C.S. and W.J.; Visualization, A.M.T. and R.K.M.; Supervision, J.C.S. and W.J.; Project administration, J.C.S. and W.J.; Funding acquisition, W.J. All authors have read and agreed to the published version of the manuscript.

**Funding:** This work was supported by the Technology Innovation Program (RS-2023-00235844, Development of nano-structured materials and devices for super steep subthreshold swing), funded by the Ministry of Trade, Industry & Energy (MOTIE, Korea) (1415187621). This work was also financially supported by the National Research Foundation of Korea, South Korea (NRF-2020R1A2C1015206, NRF-2022M3I8A2085429).

**Data Availability Statement:** The original contributions presented in the study are included in the article, further inquiries can be directed to the corresponding authors.

**Conflicts of Interest:** The authors declare no conflict of interest.

## References

1. Gautam, A.; Sk, S.; Pal, U. Recent advances in solution assisted synthesis of transition metal chalcogenides for photo-electrocatalytic hydrogen evolution. *Phys. Chem. Chem. Phys.* **2022**, *24*, 20638–20673. [[CrossRef](#)]
2. Raveendran, A.; Chandran, M.; Siddiqui, M.R.; Wabaidur, S.M.; Angaiah, S.; Dhanusuraman, R. Binary Ni–Cu nanocomposite-modified MXene-adorned 3D-nickel foam for effective overall water splitting and supercapacitor applications. *Sustainable Energy Fuels* **2024**, *8*, 1509–1525. [[CrossRef](#)]
3. Shaikh, N.; Annadata, H.V.; Mishra, A.K.; Urkude, R.R.; Mukhopadhyay, I.; Ray, A. Doping induced mixed polytypic interfaces of MoS<sub>2</sub> for superior electrocatalytic hydrogen evolution. *Appl. Surf. Sci.* **2024**, *649*, 159195. [[CrossRef](#)]
4. Zhao, S.; Zhang, C.; Wang, S.; Lu, K.; Wang, B.; Huang, J.; Peng, H.; Li, N.; Liu, M. Photothermally driven decoupling of gas evolution at the solid-liquid interface for boosted photocatalytic hydrogen production. *Nanoscale* **2024**, *16*, 152–162. [[CrossRef](#)]
5. Liu, Z.Z.; Yu, N.; Fan, R.-Y.; Dong, B.; Yan, Z.-F. Design and multilevel regulation of transition metal phosphides for efficient and industrial water electrolysis. *Nanoscale* **2024**, *16*, 1080–1101. [[CrossRef](#)]
6. Sharma, S.; Paul, A. One-pot synthesis of CoFe-nanomesh for oxygen evolution reaction. *ACS Appl. Nano Mater.* **2024**, *7*, 8567–8857. [[CrossRef](#)]
7. Li, X.; Zhao, L.; Yu, J.; Liu, X.; Zhang, X.; Liu, H.; Zhou, W. Water splitting: From electrode to green energy system. *Nano-Micro Lett.* **2020**, *12*, 131. [[CrossRef](#)]
8. Wu, Y.-H.; Janák, M.; Abdala, P.M.; Borca, C.N.; Wach, A.; Kierzkowska, A.; Donat, F.; Huthwelker, T.; Kuznetsov, D.A.; Müller, C.R. Probing surface transformations of lanthanum nickelate electrocatalysts during oxygen evolution reaction. *J. Am. Chem. Soc.* **2024**, *146*, 11887–11896. [[CrossRef](#)]
9. Paladugu, S.; Abdullahi, I.M.; Singh, H.; Spinuzzi, S.; Nath, M.; Page, K. Mesoporous Re<sub>0.5</sub>Ce<sub>0.5</sub>O<sub>2-x</sub> fluorite electrocatalysts for the oxygen evolution reaction. *ACS Appl. Mater. Interfaces* **2024**, *16*, 7014–7025. [[CrossRef](#)]
10. Li, R.; Chen, L.; Zhang, H.; Humayun, M.; Duan, J.; Xu, X.; Fu, Y.; Bououdina, M.; Wang, C. Exceptional green hydrogen production performance of a ruthenium-modulated nickel selenide. *Nanoscale* **2023**, *15*, 19604–19616. [[CrossRef](#)]
11. Qiao, Y.; Wang, F.; Guo, W.; He, Z.; Yao, L.; Li, J.; Sun, N.; Wang, Y.; Wang, F. Monolayer MoS<sub>2</sub> as a sensitive probe: Exploring the resistive switching mechanism of MoS<sub>2</sub>/NSTO heterostructures. *J. Alloys Compd.* **2023**, *967*, 171712. [[CrossRef](#)]
12. Choi, S.; Oh, G.H.; Kim, T.W.; Hong, S.; Kim, A. Radiation induced changes in chemical and electronic properties of few-layer MoS<sub>2</sub> and MoTe<sub>2</sub> films. *Appl. Surf. Sci.* **2024**, *652*, 159282. [[CrossRef](#)]
13. Ahmed, B.; Anjum, D.H.; Hedhili, M.N.; Alshareef, H.N. Mechanistic insight into the stability of HfO<sub>2</sub>-coated MoS<sub>2</sub> nanosheet anodes for sodium ion batteries. *Small* **2015**, *11*, 4341–4350. [[CrossRef](#)] [[PubMed](#)]
14. Yu, P.; Luo, F.; Chen, S. Porous MoP<sub>2</sub>/MoS<sub>2</sub> hierarchical nanowires for efficient hydrogen evolution reaction in full pH range. *J. Alloys Compd.* **2024**, *985*, 174024. [[CrossRef](#)]
15. Dighole, R.P.; Munde, A.V.; Mulik, B.B.; Dhawale, S.C.; Sathe, B.R. Multiwalled carbon nanotubes decorated with molybdenum sulphide (MoS<sub>2</sub>@MWCNTs) for highly selective electrochemical picric acid (PA) determination. *Appl. Surf. Sci.* **2024**, *659*, 159856. [[CrossRef](#)]
16. Gui, T.; Xia, X.; Wei, B.; Zhang, J.; Zhang, K.; Li, Y.; Chen, W.; Yu, W.; Cui, N.; Mu, H.; et al. In-situ fabrication of PtSe<sub>2</sub>/MoS<sub>2</sub> van der Waals heterojunction for self-powered and broadband photodetector. *Mater. Des.* **2024**, *238*, 112722. [[CrossRef](#)]
17. Xiong, H.; Nie, X.; Zhao, L.; Deng, S. Engineering symmetry breaking in twisted MoS<sub>2</sub>-MoSe<sub>2</sub> heterostructures for optimal thermoelectric performance. *ACS Appl. Mater. Interfaces* **2024**, *16*, 25124–25135. [[CrossRef](#)]
18. Jacobo, J.-R.; Olea-Mejía, O.F.; Martínez-Hernández, A.L.; Carlos, V.-S. Optimization of the optical response of 2D MoS<sub>2</sub> materials obtained through liquid-phase exfoliation using a comprehensive multi-objective approach. *FlatChem* **2024**, *45*, 100654. [[CrossRef](#)]
19. Liang, S.; Zheng, L.-J.; Song, L.-N.; Wang, X.-X.; Tu, W.-B.; Xu, J.-J. Accelerated confined mass transfer of MoS<sub>2</sub> 1D nanotube in photo-assisted metal-air batteries. *Adv. Mater.* **2024**, *36*, 2307790. [[CrossRef](#)]
20. Wang, Y.; Gao, T.; Li, R.; Chen, Y.; Luo, W.; Wu, Y.; Xie, Y.; Wang, Y.; Zhang, Y. Layered deposited MoS<sub>2</sub> nanosheets on acorn leaf like CdS as an efficient anti-photocorrosion photocatalyst for hydrogen production. *Fuel* **2024**, *368*, 131621. [[CrossRef](#)]
21. Kaushik, R.; Nandi, S.; Mandal, M.; Gupta, A.N. Biocompatible L-cysteine-capped MoS<sub>2</sub> nanoflowers for antibacterial applications: Mechanistic insights. *ACS Appl. Nano Mater.* **2024**, *7*, 7753–7765. [[CrossRef](#)]
22. Park, D.; Kim, H.; Kim, N. Enhancing valley polarization of a MoS<sub>2</sub> zigzag nanoribbon using double magnetic barriers. *Phys. E* **2024**, *159*, 115910. [[CrossRef](#)]

23. Xu, Y.; Cheng, J.; Ding, L.; Lv, H.; Zhang, K.; Hu, A.; Yang, X.; Sun, W.; Mao, Y. Interfacial engineering for promoting charge transfer in MoS<sub>2</sub>/CoFeLDH heterostructure electrodes for overall water splitting. *Int. J. Hydrogen Energy* **2024**, *49*, 897–906. [[CrossRef](#)]
24. Hai, G.; Xue, X.; Wu, Z.; Zhang, C.; Liu, X.; Huang, X. High-throughput calculation-based rational design of Fe-doped MoS<sub>2</sub> nanosheets for electrocatalytic pH-universal overall water splitting. *J. Energy Chem.* **2024**, *91*, 194–202. [[CrossRef](#)]
25. Kang, L.; Liu, S.; Zhang, Q.; Zou, J.; Ai, J.; Qiao, D.; Zhong, W.; Liu, Y.; Jun, S.C.; Yamauchi, Y.; et al. Hierarchical spatial confinement unlocking the storage limit of MoS<sub>2</sub> for flexible high-energy supercapacitors. *ACS Nano* **2024**, *18*, 2149–2161. [[CrossRef](#)] [[PubMed](#)]
26. Zou, Y.; Li, P.; Su, C.; Yan, J.; Zhao, H.; Zhang, Z.; You, Z. Flexible high-temperature MoS<sub>2</sub> field-effect transistors and logic gates. *ACS Nano* **2024**, *18*, 9627–9635. [[CrossRef](#)] [[PubMed](#)]
27. Yang, Z.J.; Li, Z.; Lampronti, G.I.; Lee, J.-I.; Wang, Y.; Day, J.; Chhowalla, M. Environmental and thermal stability of chemically exfoliated Li<sub>x</sub>MoS<sub>2</sub> for lithium-sulfur batteries. *Chem. Mater.* **2024**, *36*, 4829–4837. [[CrossRef](#)]
28. Ji, S.; Bae, S.-R.; Hu, L.; Hoang, A.T.; Seol, M.J.; Hong, J.; Katiyar, A.K.; Kim, B.J.; Xu, D.; Kim, S.Y.; et al. Perovskite light-emitting diode display based on MoS<sub>2</sub> backplane thin-film transistors. *Adv. Mater.* **2024**, *36*, 2309531. [[CrossRef](#)] [[PubMed](#)]
29. Wu, P.; Huang, M. Mechanism of adsorption and gas-sensing of hazardous gases by MoS<sub>2</sub> monolayer decorated by Pd<sub>n</sub> (n = 1–4) clusters. *Colloids Surf. A* **2024**, *695*, 134200. [[CrossRef](#)]
30. Chen, P.S.; Hu, Y.; Li, S.-Y.; Mazurkiewicz-Pawlicka, M.; Małolepszy, A. Preparation of a MoS<sub>2</sub>/carbon nanotube nanocomposite by hydrothermal method for supercapacitor. *Int. J. Electrochem. Sci.* **2024**, *19*, 100523. [[CrossRef](#)]
31. Mondal, K.G.; Rakshit, S.; Kar, B.S.; Saha, S.; Jana, P.C. Study of enhancing photocatalytic activity of solvothermal grown MoS<sub>2</sub> nanocrystals under visible light irradiation by the influence of hydrogen peroxide. *J. Photochem. Photobiol. A* **2024**, *447*, 115239. [[CrossRef](#)]
32. Al-Namshah, K.S. Synthesis of MoS<sub>2</sub>-loaded Co<sub>3</sub>O<sub>4</sub> nanocrystals for endorsed photocatalytic reduction of mercury (II) ions under visible light. *Opt. Mater.* **2023**, *142*, 114114. [[CrossRef](#)]
33. Khorasanipour, N.; Iranmanesh, P.; Saeednia, S.; Yazdi, S.T. Photocatalytic degradation of Naphthol Green in aqueous solution through the reusable ZnS/MoS<sub>2</sub>/Fe<sub>3</sub>O<sub>4</sub> magnetic nanocomposite. *Surf. Interfaces* **2023**, *36*, 102613. [[CrossRef](#)]
34. Midhun, P.S.; Kumar, K.R.; Jayaraj, M.K. Large area synthesis of mono/few-layer MoS<sub>2</sub> thin films on thermal oxide silicon substrate by pulsed laser deposition technique. *Thin Solid Films* **2023**, *782*, 140030. [[CrossRef](#)]
35. Tonon, A.; Russo, E.D.; Sgarbossa, F.; Bacci, L.; Argiolas, N.; Scian, C.; Ivanov, Y.P.; Divitini, G.; Sheehan, B.; Salvador, D.D.; et al. Laser induced crystallization of sputtered MoS<sub>2</sub> thin films. *Mater. Sci. Semicond. Process.* **2023**, *164*, 107616. [[CrossRef](#)]
36. Kim, J.H.; Kim, J.K.; Kang, Y.C. Sodium-ion storage performances of MoS<sub>2</sub> nanocrystals coated with N-doped carbon synthesized by flame spray pyrolysis. *Appl. Surf. Sci.* **2020**, *523*, 146470. [[CrossRef](#)]
37. Duraisamy, S.; Ganguly, A.; Sharma, P.K.; Benson, J.; Davis, J.; Papakonstantinou, P. One-Step hydrothermal synthesis of phase-engineered MoS<sub>2</sub>/MoO<sub>3</sub> electrocatalysts for hydrogen evolution reaction. *ACS Appl. Nano Mater.* **2021**, *4*, 2642–2656. [[CrossRef](#)]
38. Abraham, D.S.; Vinoba, M.; Bhagiyalakshmi, M. NiFe-LDH/MoS<sub>2</sub>/MXene nanocomposites as an electrode material for battery-type supercapacitors. *ACS Appl. Nano Mater.* **2024**, *7*, 5791–5801. [[CrossRef](#)]
39. Park, H.; Liu, N.; Kim, B.H.; Kwon, S.H.; Baek, S.; Kim, S.; Lee, H.-K.; Yoon, Y.J.; Kim, S. Exceptionally uniform and scalable multilayer MoS<sub>2</sub> phototransistor array based on large-scale MoS<sub>2</sub> grown by RF sputtering, electron beam irradiation, and sulfurization. *ACS Appl. Mater. Interfaces* **2020**, *12*, 20645–20652. [[CrossRef](#)]
40. Cho, Y.; Sohn, A.; Kim, S.; Hahm, M.G.; Kim, D.-H.; Cho, B.; Kim, D.-W. Influence of gas adsorption and gold nanoparticles on the electrical properties of CVD-grown MoS<sub>2</sub> thin films. *ACS Appl. Mater. Interfaces* **2016**, *8*, 21612–21617. [[CrossRef](#)]
41. Yu, N.; Ke, H.; Yu, H.; Wu, X.; Li, S.; Chen, G.; Wang, J.; Cai, N.; Xue, Y.; Yu, F. Polysulfide-induced synthesis of coral-like MoS<sub>2</sub>/NiS<sub>2</sub> nanostructures for overall water splitting. *ACS Appl. Nano Mater.* **2023**, *6*, 5136–5144. [[CrossRef](#)]
42. Yang, L.; Yuan, X.; Song, R.; Liang, W. Cu doped MoS<sub>2</sub> nanosheets/NiS<sub>2</sub> nanowires heterogeneous structure for enhanced hydrogen evolution reaction. *J. Phys. Chem. Solids* **2023**, *181*, 111540. [[CrossRef](#)]
43. Wang, Z.; Kannan, H.; Su, T.; Swaminathan, J.; Shirodkar, S.N.; Hernandez, F.C.R.; Benavides, H.C.; Vajtai, R.; Yakobson, B.I.; Meiyazhagan, A.; et al. Substitution of copper atoms into defect-rich molybdenum sulfides and their electrocatalytic activity. *Nanoscale Adv.* **2021**, *3*, 1747–1757. [[CrossRef](#)] [[PubMed](#)]
44. Lee, S.; Park, Y.; Lim, H.Y.; Son, S.; Cho, Y.; Park, J.B.; Cho, H.-S.; Jang, A.-R.; Lee, Y.-W. Bimetallic metal organic framework-derived Co<sub>9</sub>S<sub>8</sub>-MoS<sub>2</sub> nanohybrids as an efficient dual functional electrocatalyst towards the hydrogen and oxygen evolution reactions. *J. Ind. Eng. Chem.* **2024**, *130*, 317–323. [[CrossRef](#)]
45. Ghanashyam, G.; Kim, H. Co-doped 1T-MoS<sub>2</sub> microspheres embedded in N-doped reduced graphene oxide for efficient electrocatalysis toward hydrogen and oxygen evolution reactions. *J. Power Sources* **2024**, *596*, 234088. [[CrossRef](#)]
46. Zhang, Y.; Guo, H.; Song, M.; Qiu, Z.; Wang, S.; Sun, L. Hierarchical interfaces engineering-driven of the CoS<sub>2</sub>/MoS<sub>2</sub>/Ni<sub>3</sub>S<sub>2</sub>/NF electrode for high-efficient and stable oxygen evolution and urea oxidation reactions. *Appl. Surf. Sci.* **2023**, *617*, 156621. [[CrossRef](#)]
47. Abd-Elrahim, A.G.; Chun, D.-M. Nanosized Co<sub>3</sub>O<sub>4</sub>-MoS<sub>2</sub> heterostructure electrodes for improving the oxygen evolution reaction in an alkaline medium. *J. Alloys Compd.* **2021**, *853*, 156946. [[CrossRef](#)]

48. Rasool, F.; Pirzada, B.M.; Uddin, M.M.; Mohideen, M.I.H.; Yildiz, I.; Elkadi, M.; Qurashi, A. Interfacial engineering of ZnS-ZnO decorated MoS<sub>2</sub> supported on 2D Ti<sub>3</sub>C<sub>2</sub>T<sub>x</sub> MXene sheets for enhanced hydrogen evolution reaction. *Int. J. Hydrogen Energy* **2024**, *59*, 63–73. [[CrossRef](#)]
49. Liu, M.; Liu, Z.; Xiang, C.; Zou, Y.; Xu, F.; Sun, L. MoS<sub>2</sub>-CuCo<sub>2</sub>S<sub>4</sub> nanosheets with a honeycomb structure formed on Ni foam: An efficient electrocatalyst for hydrogen evolution reaction. *J. Alloys Compd.* **2024**, *988*, 174300. [[CrossRef](#)]
50. Hanslin, S.Ø.; Jónsson, H.; Akola, J. Is the doped MoS<sub>2</sub> basal plane an efficient hydrogen evolution catalyst? Calculations of voltage-dependent activation energy. *Phys. Chem. Chem. Phys.* **2023**, *25*, 15162–15172. [[CrossRef](#)]
51. Hu, W.; Liu, H.; Dong, W.; Munir, H.A.; Fan, X.; Tian, X.; Pang, L. Ammonium ions intercalated 1T/2H-MoS<sub>2</sub> with increased interlayer spacing for high-efficient electrocatalytic hydrogen evolution reaction. *J. Electroanal. Chem.* **2023**, *949*, 117882. [[CrossRef](#)]
52. Liang, J.; Yang, Y.; Zhang, J.; Dong, P.; Lou, J. Ultrasmall CoSe<sub>2</sub> Nanoparticles Grown on MoS<sub>2</sub> Nanofilms: A New Catalyst for Hydrogen Evolution Reaction. *Phys. Status Solidi RRL* **2023**, *2300169*. [[CrossRef](#)]
53. Li, C.; Zhu, L.; Wu, Z.; Chen, Q.; Zheng, R.; Huan, J.; Huang, Y.; Zhu, X.; Sun, Y. Phase engineering of W-doped MoS<sub>2</sub> by magneto-hydrothermal synthesis for hydrogen evolution reaction. *Small* **2023**, *19*, 2303646. [[CrossRef](#)] [[PubMed](#)]
54. Lu, X.; Tao, T.; Zhang, Y.; Lu, S.; Xie, J.; Ding, Z.; Wu, Z. Amidoximated polyacrylonitrile extended the interlayer spacing of MoS<sub>2</sub>/graphite for hydrogen evolution reaction. *ChemistrySelect* **2023**, *8*, e202204699. [[CrossRef](#)]
55. Yang, Y.; Zhang, K.; Lin, H.; Li, X.; Chan, H.C.; Yang, L.; Gao, Q. MoS<sub>2</sub>-Ni<sub>3</sub>S<sub>2</sub> heteronanorods as efficient and stable bifunctional electrocatalysts for overall water splitting. *ACS Catal.* **2017**, *7*, 2357–2366. [[CrossRef](#)]
56. Hanan, A.; Lakhan, M.N.; Walvekar, R.; Khalid, M.; Prakash, C. Heteroatom-doped MXenes as electrocatalysts for hydrogen evolution reaction: A review on the recent advances, mechanisms and prospects. *Chem. Eng. J.* **2024**, *483*, 149107. [[CrossRef](#)]
57. Xiao, C.; Hong, T.; Jia, J.; Jia, H.; Li, J.; Zhu, Y.; Ge, S.; Liu, C.; Zhu, G. Unlocking the potential of hydrogen evolution: Advancements in 3D nanostructured electrocatalysts supported on nickel foam. *Appl. Catal. B* **2024**, *355*, 124197. [[CrossRef](#)]
58. Cao, X.; Gao, Y.; Li, Y.; Weragoda, D.M.; Tian, G.; Zhang, W.; Zhang, Z.; Zhao, X.; Chen, B. Research progress on MOFs and their derivatives as promising and efficient electrode materials for electrocatalytic hydrogen production from water. *RSC Adv.* **2023**, *13*, 24393–24411. [[CrossRef](#)] [[PubMed](#)]
59. Xu, Y.; Fan, K.; Zou, Y.; Fu, H.; Dong, M.; Dou, Y.; Wang, Y.; Chen, S.; Yin, H.; Al-Mamun, M.; et al. Rational design of metal oxide catalysts for electrocatalytic water splitting. *Nanoscale* **2021**, *13*, 20324–20353. [[CrossRef](#)]
60. Mohanty, B.; Ghorbani-Asl, M.; Kretschmer, S.; Ghosh, A.; Guha, P.; Panda, S.K.; Jena, B.; Krasheninnikov, A.V.; Jena, B.K. MoS<sub>2</sub> quantum dots as efficient catalyst materials for the oxygen evolution reaction. *ACS Catal.* **2018**, *8*, 1683–1689. [[CrossRef](#)]
61. Muthurasu, A.; Maruthapandian, V.; Kim, H.Y. Metal-organic framework derived Co<sub>3</sub>O<sub>4</sub>/MoS<sub>2</sub> heterostructure for efficient bifunctional electrocatalysts for oxygen evolution reaction and hydrogen evolution reaction. *Appl. Catal. B* **2019**, *248*, 202–210. [[CrossRef](#)]
62. Ma, W.; Li, W.; Zhang, H.; Wang, Y. N-doped carbon wrapped CoFe alloy nanoparticles with MoS<sub>2</sub> nanosheets as electrocatalyst for hydrogen and oxygen evolution reactions. *Int. J. Hydrogen Energy* **2023**, *48*, 22032–22043. [[CrossRef](#)]
63. Rong, J.; Ye, Y.; Cao, J.; Liu, X.; Fan, H.; Yang, S.; Wei, M.; Yang, L.; Yang, J.; Chen, Y. Restructuring electronic structure via W doped 1T MoS<sub>2</sub> for enhancing hydrogen evolution reaction. *Appl. Surf. Sci.* **2022**, *579*, 152216. [[CrossRef](#)]
64. Younis, A.; Sehar, S.; Guan, X.; Aftab, S.; Manaa, H.; Mahmood, T.; Iqbal, J.; Akram, F.; Ali, N.; Wu, T. Four-in-one strategy to boost the performance of 3-dimensional MoS<sub>2</sub> nanostructures for industrial effluent treatment and hydrogen evolution reactions. *J. Alloys Compd.* **2024**, *976*, 173104. [[CrossRef](#)]
65. Homayounfard, A.M.; Maleki, M.; Ghanbari, H.; Kahnamouei, M.H.; Safaei, B. Growth of few-layer flower-like MoS<sub>2</sub> on heteroatom-doped activated carbon as a hydrogen evolution reaction electrode. *Int. J. Hydrogen Energy* **2024**, *55*, 1360–1370. [[CrossRef](#)]
66. Huang, W.-H.; Li, X.-M.; Yang, X.-F.; Zhang, H.-B.; Wang, F.; Zhang, J. Highly efficient electrocatalysts for overall water splitting: Mesoporous CoS/MoS<sub>2</sub> with hetero-interfaces. *Chem. Commun.* **2021**, *57*, 4847–4850. [[CrossRef](#)] [[PubMed](#)]
67. Khan, N.A.; Rahman, G.; Chae, S.Y.; Shah, A.U.H.A.; Joo, O.S.; Mian, S.A.; Hussain, A. Boosting electrocatalytic hydrogen generation from water splitting with heterostructured MoS<sub>2</sub>/NiFe<sub>2</sub>O<sub>4</sub> composite in alkaline media. *Int. J. Hydrogen Energy* **2024**, *69*, 261–271. [[CrossRef](#)]
68. Liu, W.; Dong, J.; An, B.; Su, H.; Teng, Z.; Li, N.; Gao, Y.; Ge, L. Synergistic dual built-in electric fields in 1T-MoS<sub>2</sub>/Ni<sub>3</sub>S<sub>2</sub>/LDH for efficient electrocatalytic overall water splitting reactions. *J. Colloid Interface Sci.* **2024**, *673*, 228–238. [[CrossRef](#)]

**Disclaimer/Publisher's Note:** The statements, opinions and data contained in all publications are solely those of the individual author(s) and contributor(s) and not of MDPI and/or the editor(s). MDPI and/or the editor(s) disclaim responsibility for any injury to people or property resulting from any ideas, methods, instructions or products referred to in the content.